

Convergence of the method of the hyperspherical \mathcal{R} matrix with semiclassical outgoing waves

P. Selles, L. Malegat, and A. Huetz

*Laboratoire d'Interaction du Rayonnement X avec la Matière (Laboratoire associé au CNRS), Université Paris-Sud,
91405 Orsay, France*

A. K. Kazansky

Fock Institute of Physics, The University of St. Petersburg, 198504, Russia

S. A. Collins

Department of Physics, University of Newcastle, Newcastle upon Tyne, NE1 7RU, United Kingdom

D. P. Seccombe and T. J. Reddish

Department of Physics, University of Windsor, Windsor, Ontario, Canada N9B 3P4

(Received 14 November 2003; published 12 May 2004)

A systematic study is reported on the convergence of computed triply differential cross sections for photo-double ionization of helium at 20 and 25 eV above threshold, obtained using the hyperspherical \mathcal{R} matrix with semiclassical outgoing waves method. Such a study has become feasible due to an essential improvement in the description of the radial correlation coordinate $\alpha = \arctan(r_2/r_1)$ at short range, and to the implementation of the code on a more powerful computer. It shows that the size requirements of the inner region $R \leq R_0$, with $R = \sqrt{r_1^2 + r_2^2}$, vary considerably depending on the dynamic situation considered. Typically, while $R_0 \approx 20$ a.u. proves sufficient in most circumstances, one has to increase the inner region up to $R_0 \approx 60$ a.u. in order to reach convergence in the triply differential cross sections obtained for very asymmetric energy sharings or in the particular case when one electron is ejected along the electric field for linearly polarized photons. The converged calculations are generally in very good agreement with new experimental data of high statistical quality recorded in the latter case, at 25 eV above threshold, for various energy sharings. The dynamic situations identified here call for further experimental and theoretical studies.

DOI: 10.1103/PhysRevA.69.052707

PACS number(s): 32.80.Fb

I. PRESENT STATE OF THEORETICAL AND EXPERIMENTAL STUDIES OF PHOTO-DOUBLE-IONIZATION OF HELIUM

Extended sets of theoretical and experimental data on the double electronic continuum have accumulated in the 1990s, covering a large variety of dynamic and kinematic conditions. Here, we focus on the prototypical process of photo-double-ionization (PDI) of helium, paying special attention to the low-energy triply differential cross sections (TDCSs) which carry the most detailed information on the correlated dynamics of the two escaping electrons.

On the experimental side, the PDI of ground-state helium has been widely studied. PDI studies for helium have benefited from considerable technical advances in the last ten years. For example, spectrometers that employ position-sensitive detectors now enable the simultaneous detection of many coincidence events, thus increasing the detection efficiency by an order of magnitude. Moreover, the COLTRIMS (cold-target recoil-ion momentum spectroscopy) technique allows absolute values of the cross sections to be readily determined. As a result, a very large set of TDCSs covering a variety of dynamic situations is now available. Most of these TDCSs are relative [1–6], some are relative but inter-normalized [7], and a few are absolute [8–11]. The first absolute measurements of TDCSs were obtained in 1995 by a direct and self-consistent method [8]. The COLTRIMS technique began to provide absolute TDCSs in 1998 with the

well-known data of Braüning *et al.* [9] recorded at an excess energy of 20 eV. Although some of the individual TDCSs have significant scatter in the data, the whole data set has nevertheless acted as the benchmark for comparison with theoretical calculations. Since then few absolute experimental TDCSs have been produced. The first ones [10], performed at the very low excess energy of 0.1 eV, have not yet been reproduced by any *ab initio* theory. The second ones are those of Achler *et al.* [11], obtained at the same excess energy as those of Braüning *et al.* but for a different light polarization state and with significantly improved statistics.

On the theoretical side, a comprehensive overview of the most outstanding contributions to the description of the double escape dynamics can be found in the work of Malegat [12]. Here we focus on the most recent methods that have in common to deal with the full complexity of the three-body Coulomb problem, treating the two electrons as genuinely equivalent: the time-dependent close coupling (TDCC), the exterior complex scaling (ECS), and the hyperspherical \mathcal{R} matrix with semiclassical outgoing waves (HRM-SOW) methods. The ECS method has been extensively applied to the electron-impact ionization of hydrogen [13–17]. Very recently, it has been used to describe the PDI of helium as well, but the results have not been published yet. Consequently, this method will not be discussed in the course of this paper. A review of ECS calculations is available in Ref. [18]. On the opposite, both the TDCC [19] and HRM-SOW [21,22] calculations were first validated by comparison with the

above-mentioned benchmark absolute measurements of Braüning *et al.* [9]. Thereafter, the TDCC results were compared [20] with relative experimental data of higher statistics recorded for linearly polarized light at 25 eV [4], 40 eV [2,7], and 60 eV [3] excess energies. Similarly, the HRM-SOW calculations were compared with data obtained at 60 eV above threshold for elliptically polarized light [5], at 25 eV above threshold for linearly polarized light [6], and very recently at 40 eV above threshold for linearly polarized light [7,23,24], as well as at 20 eV using elliptically polarized light [25].

All these comparative studies of theoretical and experimental TDCSs generally emphasize good, or even excellent, overall agreement both in shape and in magnitude. However, if one looks into the details of the results, one realizes that in some circumstances the level of agreement could be improved. Disagreements have been observed between the absolute values of the cross sections given by the different theories in cases when only relative measurements are available. The TDCSs obtained by TDCC [20] and HRM-SOW [23] at 40 eV [7], for instance, differed initially by a factor 2, for which TDCC has been only recently corrected [24]. Significant differences in the shapes of theoretical and experimental TDCSs are also apparent in some cases. In the work of Colgan and Pindzola [20], for instance, the level of agreement with the experimental TDCSs of Cvejanović *et al.* [2] deteriorates when one electron is detected along the direction of the electric field under unequal energy sharing conditions. Similarly, in the experimental conditions of Bolognesi *et al.* [7], when the electron of higher energy is detected along the direction of the electric field, both TDCC [20] and HRM-SOW [23,24] TDCSs exhibit a quasi-one maximum structure while experimental data indicate the existence of three equivalent peaks [24].

Further theoretical work is obviously required. Accordingly, we present here a systematic convergence study of an improved implementation of the HRM-SOW method. One of our purposes is to reanalyze the dynamic situations that have proven to be the most challenging for the theory in the case of linear polarization: namely, those characterized by asymmetric sharing of the energy and the ejection of one electron along the direction of the electric field. We also present new TDCS measurements at 25 eV, taken in these conditions, which extend those published earlier [6].

The paper is organized as follows. Section II is devoted to a presentation of the main tools and principles of the HRM-SOW method, in order to highlight those parameters that control the accuracy of the calculation. The third section presents an improved description of the dependence of the $^1P^0$ double-continuum wave function on the radial correlation angle α which is essential to make convergence studies feasible. Fully integrated and triply differential cross sections are displayed in Secs. IV and V, respectively, as an illustration of the convergence rate of our method. Also in Sec. V comparisons between extended experimental TDCSs and the most recent HRM-SOW results are presented. Conclusions are drawn in Sec. VI.

II. THE HRM-SOW METHOD

The HRM-SOW method has been described in detail in two earlier publications [21,22]. Only the main features nec-

essary to understand this convergence study will be recalled here. The basic equation for the description of the PDI of helium by the HRM-SOW method is the stationary inhomogeneous Schrödinger equation

$$[H(\vec{r}_1, \vec{r}_2) - E]\Phi_E(\vec{r}_1, \vec{r}_2) = \Phi_0(\vec{r}_1, \vec{r}_2), \quad (1)$$

which has to be solved for the outgoing wave boundary conditions. In Eq. (1), \vec{r}_1, \vec{r}_2 , are the radius vectors of the electrons with respect to the nucleus, H is the two-electron Hamiltonian, E is the excess energy above threshold, and $\Phi_E(\vec{r}_1, \vec{r}_2)$ is the photoabsorption wave function. The source term on the right-hand side is given by

$$\Phi_0(\vec{r}_1, \vec{r}_2) = -\frac{1}{2}\vec{\epsilon}_0 \cdot \vec{D}\Psi_0(\vec{r}_1, \vec{r}_2), \quad (2)$$

where $\vec{\epsilon}_0$ is the amplitude of the electric-field vector, \vec{D} is the dipole operator, and $\Psi_0(\vec{r}_1, \vec{r}_2)$ is the helium ground-state wave function.

Hyperspherical coordinates are used. They are composed of the hyperradius $R = \sqrt{r_1^2 + r_2^2}$, which measures the size of the system, the hyperangle $\alpha = \arctan(r_2/r_1)$, which is related to the radial correlation, and a set of four spherical angles $\theta_1, \phi_1, \theta_2, \phi_2$ locating the directions of the two outgoing electrons.

The configuration space is split into two regions. In the inner region defined by $R \leq R_0$, a full quantum \mathcal{R} matrix method is used. It is complemented by the expansion of the wave function at $R=R_0$ onto the adiabatic eigenchannels of the fixed $R=R_0$ Hamiltonian. This expansion allows one to impose outgoing wave boundary conditions in a simple way. A quantum treatment of all angles is still used in the complementary external region $R > R_0$, together with a semiclassical description of the outgoing motion in R .

The calculation then proceeds in three steps. First, the photoabsorption wave function Φ_E is extracted on the hypersphere $R=R_0$ which limits the inner region, R_0 being of the order of a few tens of a.u. Second, it is propagated in the outer region to a very large hyperradius R_∞ which is of the order of 10^5 a.u. Third, the cross sections are obtained by a straightforward computation of the outgoing flux through the hypersphere $R=R_\infty$ according to the basic laws of quantum mechanics.

The validity of each of these three steps is now discussed.

(i) While the \mathcal{R} -matrix equations are absolutely rigorous, they are complemented by a set of approximate equations that results when one neglects the R variation of the adiabatic eigenchannels at $R=R_0$ in a small interval surrounding R_0 , and imposes an outgoing wave behavior at $R=R_0$. These approximations are valid provided that R_0 is taken large enough for the R variation of the three-body potential to be very slow for $R \geq R_0$.

(ii) The propagation procedure implies first that one ignores the source term in Eq. (1). Second, that the two-electron wave function Φ_E is written as the product of a weakly R -dependent function of the five angles, by a hyper-radial semiclassical outgoing wave associated with a local momentum $p(R)$. Third, this local momentum is defined by $p(R) = \sqrt{2[E + (Z_{eff}(R)/R)]}$, the basic idea being that the ef-

fective charge $Z_{eff}(R)$ should be close to the Wannier value $Z_W=(4Z-1)/\sqrt{2}$ —with Z the nuclear charge—at large R and should ensure flux conservation at R_0 . Accordingly, $Z_{eff}(R)$ is taken as a one-parameter fractional interpolation between $Z_0=Z_{eff}(R_0)$ and Z_W . The parameter-free character of the procedure can only be maintained if these two values are close enough. These approximations are valid under conditions similar to the ones outlined in points (i).

(iii) The extraction of the cross sections requires one to disentangle the weak double-ionization channel from the dominant single-ionization channels. The ability of the method to propagate the wave function up to macroscopic hyperradii allows one to confine the significant single-ionization channels in vanishing angular sectors located around $\alpha=0$ and $\pi/2$. The width of these sectors can be evaluated as $\Delta\alpha(n_{max},R)=r_{n_{max}}/R$, where $r_{n_{max}}\simeq(0.75n_{max}^2)$ a.u. measures the extension of the highest Rydberg state $\text{He}_{n=n_{max}}^+$ that can be significantly excited in the photoabsorption. According to Bizau and Wuilleumier [26], at an excess energy above threshold of about 20 eV, $n_{max}=5$ can be considered as a reasonable order of magnitude, so that the single ionization is confined in sectors of about 2×10^{-3} rad width at a distance of 10^4 a.u. As a result, the accurate evaluation of the cross sections from their very definition, based on the flux of the wave function, is possible. This is a distinctive feature of the HRM-SOW method.

The convergence of the TDCSs with respect to (a) the dimensions of the various basis sets or grid representations used, (b) the outer region propagation step, and (c) R_∞ , has been checked carefully for all published HRM-SOW data which were obtained up to now with inner regions of moderate size ($10\text{ a.u.} < R_0 < 25\text{ a.u.}$). The convergence with respect to R_∞ was also illustrated in detail in Ref. [22]. Thus only one item remains to be systematically investigated: namely, the convergence with respect to an increase of the size of the inner region, which will test the range of validity of the approximations (i) and (ii) underlying the HRM-SOW method. To this end, a more efficient representation of the inner region is required in order to keep the computational requirements compatible with resources currently available.

III. IMPROVED REPRESENTATION OF THE $1p^0$ DOUBLE CONTINUUM WAVE FUNCTION IN THE INNER REGION

The representation used in previous HRM-SOW calculations [21,22] was based on n_ℓ gerade and ungerade bipolar harmonics $g,uY_{\ell\ell+1}^{10}$, ℓ ranging from 0 to $n_\ell-1$, and on a Lagrange-Jacobi mesh representation of dimension n_R for the variable R . The dependence on the radial correlation coordinate α was expanded, within each ℓ subspace, on n_α gerade and ungerade functions:

$${}^g\omega_n^\ell(\alpha) = (\sin \alpha \cos \alpha)^{\ell+1} \cos 4n\alpha, \quad n = 0, \dots, n_\alpha - 1, \quad (3a)$$

$${}^u\omega_n^\ell(\alpha) = (\sin \alpha \cos \alpha)^\ell \sin 4n\alpha, \quad n = 1, \dots, n_\alpha. \quad (3b)$$

These functions are gerade and ungerade Fourier basis functions defined on the $[0, \pi/2]$ interval of definition of α , modified to incorporate the expected $\alpha^{\ell+1}[(\pi/2-\alpha)^{\ell+1}]$ behavior of the solution in vicinity of the boundary $\alpha=0$ [$\alpha=\pi/2$]. As such, they are associated with an α grid of constant step size $\delta\alpha=\pi/2n_\alpha$.

The first published results were obtained for $R_0=10$ a.u. with $n_\ell=5$, $n_\alpha=40$, and $n_R=15$. The dimension of the full representation was then 6000, and the main numerical task, which consisted in diagonalizing a 6000×6000 matrix, was completed on a simple PC (PIII 450 MHz 768 Mb RAM).

As the dimension of such a representation has to be evaluated for a size of the inner region increasing up to $R_0=60$ a.u., the following points should be considered. First, the number of partial waves required, n_ℓ , is expected to increase slowly with R_0 in the 10–60 a.u. domain. This assumption is based on what happens in the implementation of the HRM-SOW method in the outer region: the propagation up to distances of 10^5 a.u. only requires about 25 partial waves. However, since the $n_\ell=5$ used previously was in fact higher than necessary ($n_\ell=3$ was sufficient), $n_\ell=5$ is a reasonable guess to obtain a crude evaluation of the dimension of the representation. Second, our experience has taught us that the dimension n_R of the Lagrange-Jacobi mesh representation increases linearly with R_0 . Finally, concerning the adaptation of n_α , a significant increase is foreseen. Indeed, as R becomes larger and larger, the 3-body potential exhibits steeper and steeper wells in the vicinity of $\alpha=0$ and $\alpha=\pi/2$ [27]. Moreover, the dynamics must be represented carefully in those regions, where a strong competition between single and double photoionization takes place. More quantitatively, as the divergent terms in the potential are of the form $-2/R\alpha$ in the vicinity of $\alpha=0$ or $-2/R(\pi/2-\alpha)$ in the vicinity of $\alpha=\pi/2$, maintaining a constant accuracy is equivalent to keeping $R_0 \delta\alpha$ constant. This requires that n_α varies linearly with R_0 .

Following these guidelines, the matrix to diagonalize is expected to be about $216\,000\times 216\,000$ for $R_0=60$ a.u. Storing this matrix would require as much as 364 Gb, a memory allocation that is one order of magnitude larger than that currently available to us at the CNRS computer center IDRIS (Orsay, France). Diagonalizing it using general routines, the runtime of which scales as N^3 , would require about six months of computing time at this facility. So, clearly, the representation used has to be optimized. This has been done, thanks to a substantial improvement in the α representation. Namely, the variable α has been substituted by the variable x such that

$$\alpha = \frac{\pi}{4}(1 - \cos 2x) \quad (4)$$

and an x basis of the form given by Eqs. (3a) and (3b) has been used. Thus, the Fourier series in the variable x correspond to a constant step in x , but to a variable step in α , with a much higher density of representative points in the critical regions around $\alpha=0$ and $\alpha=\pi/2$, and an equivalent density

in the vicinity of $\alpha = \pi/4$. More quantitatively, $\delta\alpha \approx \pi/2\delta x^2$ in the vicinity of $\alpha = 0$ or $\pi/2$ and $\delta\alpha \approx \pi/2\delta x$ in the vicinity of $\alpha = \pi/4$. As a result of this simple substitution, the convergence rate of the inner region calculation with respect to the size of the α representation has been improved by an order of magnitude.

This has allowed us to run HRM-SOW calculations for much larger inner regions than before. In the largest case considered here, for which $R_0 = 60$ a.u., the dimension of the matrix to consider is 27 000, corresponding to $n_\ell = 5$, $n_R = 90$, and $n_x = 30$. The storage and diagonalization of that matrix require about 6 Gb memory and 8 h CPU, respectively, on the CNRS computer center IDRIS in Orsay, using the general LAPACK diagonalization routines.

IV. CONVERGENCE OF THE FULLY INTEGRATED CROSS SECTIONS EXTRACTED AT R_0

Important insights into the convergence rate of the HRM-SOW method with respect to R_0 can be obtained by considering the evolution of the physical quantities extracted on the hypersphere $R = R_0$. These investigations have been performed for R_0 increasing from 10 to 60 a.u. and within the excess energy range 20–60 eV. Within this range, the trends observed do not depend on the excess energy. Therefore they are illustrated here at the single excess energy of 25 eV.

The first quantity that can be extracted at $R = R_0$ is the total (single+double) ionization cross section that is directly related to the total outgoing flux. This cross section varies by less than 1% as R_0 increases from 10 to 30 a.u. and then remains fixed when R_0 is increased any further. This shows that the source term is still active—although very weakly—up to 30 a.u. The converged theoretical value of 368.5 kb is slightly above the experimental determination [26] of 360 ± 6 kb.

The outgoing flux in the first adiabatic channel can also be computed. The corresponding cross section varies from 320 kb at $R_0 = 10$ a.u. to 330 kb at $R_0 = 60$ a.u. and is in excellent agreement with the 319 ± 7 kb experimental determination [26] of the single-ionization cross sections to $\text{He}_{n=1}^+$, noted $\sigma_{n=1}^+$. Consistently, the energy of the first adiabatic channel corresponds to that of $\text{He}_{n=1}^+$ perturbed by a negative charge placed at a distance R_0 with an accuracy that varies from 0.3% at $R_0 = 10$ a.u. to 0.07% at $R_0 = 60$ a.u. The accuracy of the energy and cross section obtained as soon as $R_0 = 10$ a.u. reflects the rapid decoupling of the channel associated with single ionization to $\text{He}_{n=1}^+$ from all other competing channels. This allows the subtraction of the first adiabatic channel from the wave function at R_0 before propagating through the outer region. This procedure, already used by Selles *et al.* [22] and discussed in detail by Malegat *et al.* [23], proved essential for obtaining Z_0 values close to the Wannier value $Z_W = 4.95$.

Importantly, the single-ionization cross section to $\text{He}_{n=2}^+$, denoted $\sigma_{n=2}^+$, can also be calculated from $R_0 = 20$ a.u. upwards. The sum of the fluxes into the second to fourth adiabatic channels gives a cross section in very good agreement with the experimental value of $\sigma_{n=2}^+$. Namely, the computed

value is 22 kb at $R_0 = 20$ a.u., decreasing slowly to 21 kb at $R_0 = 60$ a.u., in excellent agreement with the experimental determination of 23 ± 2 kb [26]. Consistently, the energies of the second to fourth adiabatic channels merge into those of the Stark levels of $\text{He}_{n=2}^+$ perturbed by a negative charge placed at a distance R_0 . For example, at $R_0 = 60$ a.u., the adiabatic energies are -0.5159 , -0.5167 , -0.5171 a.u., in excellent agreement with the first-order Stark levels lying at -0.5163 , -0.5167 , and -0.5171 a.u. [28]. As a result, these three additional adiabatic channels can be excluded from the wave function before propagation in the outer region, as done previously with the first adiabatic channel. This is even highly desirable, as the effective charge Z_0 obtained without subtraction of the second to fourth adiabatic channels is about 8, 11, 14, 17, and 19 at $R_0 = 20, 30, 40, 50,$ and 60 a.u., respectively. From $R_0 = 30$ a.u., these values are too far from the Wannier value $Z_W = 4.95$ to maintain the parameter-free character of our approach, as discussed in Sec. II. With subtraction of the next three channels, Z_0 takes the values 4.9, 5.3, 5.1, 6, and 7.2, which remain close enough to Z_W even for the highest value of R_0 .

Finally, let us emphasize that at $R_0 = 60$ a.u., the sum of the fluxes in the fifth to ninth adiabatic channels leads to a cross section of 3.6 kb, compared to the experimental value 3.8 ± 0.5 kb [26] of $\sigma_{n=3}^+$. Significantly, such excellent agreement between theory and experiment is achieved for a quantity that is only 1% of the total ionization cross section, but of the same order of magnitude as the total double-ionization cross section. The energies of these five adiabatic channels correspond to the Stark levels of the perturbed $\text{He}_{n=3}^+$ ion with an accuracy better than 0.15%. Subtracting them from the wave function leads to a Z_0 value of 5.6, while retaining them leads to 7.2, both values being reasonably close to Z_W . For $R_0 = 60$ a.u., calculations have been performed, either subtracting these five channels before propagation or retaining them. The resulting TDCSs are perfectly superimposable in all the dynamic situations studied.

V. CONVERGENCE OF THE TDCS EXTRACTED AT R_∞

A. Dynamic conditions

TDCSs at the nearby excess energies of 20 and 25 eV have been calculated for the experimental conditions of Achler *et al.* [11] and for those of our experiments, respectively. These two sets of data present high statistics and cover a large range of energy sharings. They also display interesting complementary properties: Achler *et al.*'s measurements have the great advantage of being absolute, while our relative measurements were taken for a specific class of dynamic situations which are particularly challenging to the theory.

Achler *et al.* [11] have used the COLTRIMS technique at the Photon Factory, Tsukuba, to obtain TDCSs in the “perpendicular geometry,” i.e., in the plane perpendicular to the photon beam, with left and right elliptically polarized light. Pure left and right circular TDCSs have then been extracted for four energy sharings, $E_1/E_2 = 1.0, 2.64, 7.0,$ and 39.0 , going from equal sharing to a very asymmetric one. They solely depend on the interelectronic azimuthal angle $\phi_2 - \phi_1$.

We used a toroidal multidetection technique at SUPERACO, Orsay, to measure the TDCSs in the ‘‘coplanar geometry,’’ i.e. in the plane containing the photon beam and the electric field associated with the linearly polarized light. The electrons are located by their azimuthal angles in the detection plane, measured from the polarization axis. The experiment focuses on the case when one electron, say ‘‘electron 1,’’ is detected along the electric-field direction, i.e. at $\varphi_1=0^\circ$, and the energy is shared asymmetrically between the two electrons. The first series of measurements studied the energy sharings $E_2/E_1=24, 11.5, 4$, and 2.57 [6]. We present in this work results for the reverse situation where electron 1 has the highest energy, i.e., $E_1/E_2=11.5, 4$, and 2.57 .

B. Convergence parameters

For each R_0 value from 10 to 60 a.u., the convergence of the TDCSs with respect to the size of the representation has been studied systematically. It has been determined that convergence is achieved for $n_\ell=5$, $n_R=1.5R_0$, and $n_x=15, 20, 25, 30$, and 30 for $R_0=20, 30, 40, 50$, and 60 a.u., respectively. The TDCSs proved insensitive to a simultaneous increase of n_ℓ by 2, n_R by 5, and n_x by 5. These results are consistent with the predictions made in Sec. III: the evolution of n_R with R_0 is linear, that of n_x is such that R_0/n_x^2 is approximatively constant, and the number of partial waves required remains as low as $n_\ell=5$, independent of R_0 in the 20–60 a.u. range.

C. Convergence studies with respect to R_0 at 20 eV

Figure 1 is devoted to the $E=20$ eV results.¹ The first characteristic to be emphasized is that, in the four energy sharing cases, the location of the peaks is essentially constant above $R_0=10$ a.u. The positions effectively fluctuate by less than 2% when R_0 is gradually increased up to 60 a.u. The second property is the excellent agreement between the absolute experimental TDCSs and the absolute HRM-SOW TDCSs obtained at $R_0=60$ a.u. Accordingly, the latter can be taken as a reference to evaluate the relative deviations of the magnitude of the main peak as R_0 varies from 10 to 50 a.u. These deviations denoted by $\Delta\sigma_M^{(3)}/\sigma_M^{(3)}$ are plotted in Fig. 2 versus $[N(R_0)]^3$ where $N(R_0)=2n_\ell n_x n_R$ is the dimension of the representation used in the inner region for a given R_0 value. As the inner region \mathcal{R} -matrix treatment requires the diagonalization of an $N\times N$ matrix, the run time of which scales as N^3 , the plot of Fig. 2 relates the accuracy obtained with the associated computational cost. First of all this figure shows that the deviation observed never exceeds 25%. Second, the four curves exhibit a slow oscillatory convergence pattern, leading, at $R_0=50$ a.u., to accuracies that depend on the energy sharing: about 15% for the most asymmetric one, less than 5% for the others. This is because the semiclassical treatment of the R motion implemented in the external region is not perfectly adapted to the description of the single-ionization channels, due to the fundamentally quantal nature

¹Please note an error in Fig. 1 of Ref. [25]: the TDCS is reported to be in $\text{b}/\text{eV}/\text{sr}^2$, although it should be in 10^{-5} a.u.

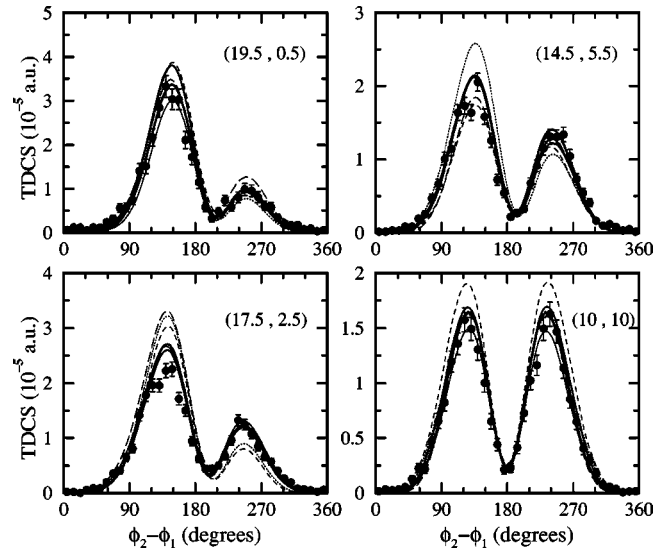


FIG. 1. TDCSs for PDI of He obtained at 20 eV above threshold in the perpendicular geometry using left circularly polarized light (in 10^{-5} a.u.), versus $\phi_2 - \phi_1$ (in degrees). The energies (E_1, E_2) (in eV) are specified on each panel. Absolute measurements [11], dots with error bars. Present absolute HRM-SOW calculations for $R_0 = 10$ a.u., dotted line; $R_0=20$ a.u., short dashed line; $R_0=30$ a.u., long dashed line; $R_0=40$ a.u., thin continuous line; $R_0=50$ a.u., medium continuous line; $R_0=60$ a.u., thick continuous line.

of the bound ionic states. More precisely, for any energy sharing $\alpha = \arctan\sqrt{E_2/E_1}$, a critical distance R_C exists below which α falls within the angular sector $\Delta\alpha(n_{max}, R)$ where single ionization dominates. If R_C is larger than R_0 , the relevant single-ionization channels $n \leq n_{max}$ are treated in part semiclassically from R_0 to R_C , causing inaccuracies in the wave function about the α value of interest. These inaccuracies propagate to R_∞ and affect the final results. Accordingly, the computed cross sections vary with increasing R_0 until $R_0=R_C$, when they reach stable and accurate values. Figure 3 illustrates this situation. Estimating, as in Sec. II, that $n_{max}=5$, Fig. 3 shows that convergence should be obtained at $E_1=E_2$ ($\alpha=45^\circ$) from $R_0=25$ a.u., at $E_1/E_2=2.64$ ($\alpha=32^\circ$) from $R_0=34$ a.u., at $E_1/E_2=7$ ($\alpha=21^\circ$) from $R_0=51$ a.u., and at $E_1/E_2=39$ ($\alpha=9^\circ$) far beyond 60 a.u. The actual conver-

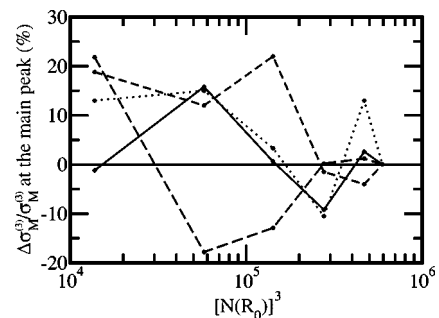


FIG. 2. $\Delta\sigma_M^{(3)}/\sigma_M^{(3)}$ at the main peak (in percent) versus the dimension $[N(R_0)]^3$ of the representation used in the hypersphere $R \leq R_0$, for the four energy sharing cases represented in Fig. 1. Dotted line, $E_1=19.5$ eV; short dashed line, $E_1=17.5$ eV; long dashed line, $E_1=14.5$ eV; continuous line, $E_1=10$ eV.

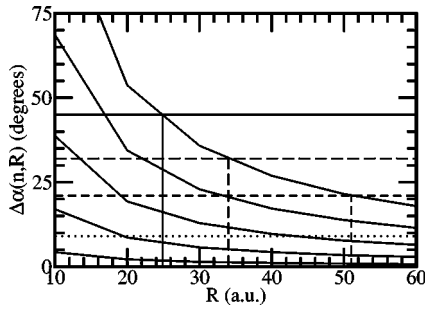


FIG. 3. Confinement range $\Delta\alpha(n,R)$ of single ionization to He_n^+ (in degrees) versus R (in a.u.), for $n=1$ (bottom curve) to $n=5$ (top curve). Horizontal lines are plotted at the α values associated asymptotically to the energy sharings considered in the previous figures, with the same conventions as in Fig. 2.

gence properties of our method seem to indicate that 5 might be an overestimation of n_{max} : they are obviously more consistent with $n_{max}=4$.

D. Convergence studies with respect to R_0 at 25 eV

Figures 4–7 are devoted to $E=25$ eV. Figures 4 and 5, and the left and middle columns of Fig. 6 exhibit theoretical TDCSs computed for increasing values of R_0 from 10 to 60 a.u. at $\varphi_1=90^\circ$, 30° , and 0° , respectively. These TDCSs are plotted versus the interelectronic angle, measured from the direction of emission of electron 1 to the direction of emission of electron 2, covering the full plane in the $[0, 2\pi]$ range. In the left and middle columns of Fig. 7 the experimental TDCSs measured at $\varphi_1=0^\circ$ are compared with the converged theoretical results at $R_0=60$ a.u. Each row of Figs. 4 and 5 and each row of the left and middle columns of Figs.

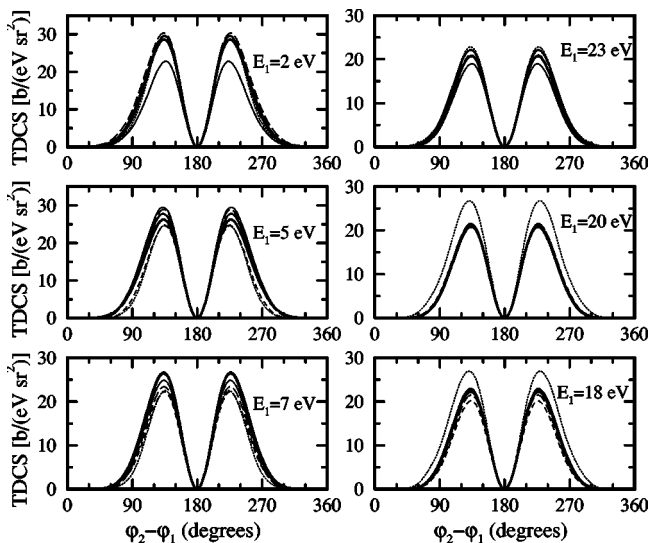


FIG. 4. TDCSs for PDI of helium obtained at 25 eV above threshold in the coplanar geometry using linearly polarized light (in $\text{b}/\text{eV}/\text{sr}^2$) versus $\varphi_2-\varphi_1$ (in degrees) for $\varphi_1=90^\circ$. The energy of electron 1 is specified on each panel. The six lines represent absolute H $\overline{\text{R}}\text{M}$ -SOW calculations for six values of R_0 with the conventions of Fig. 1.

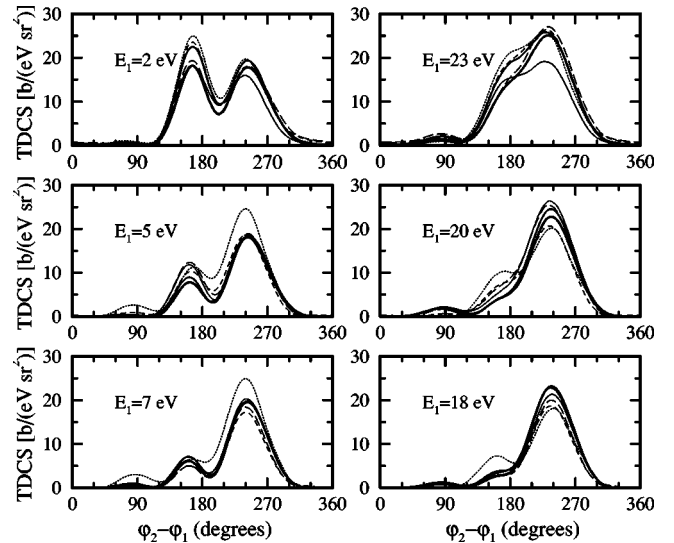


FIG. 5. Same as Fig. 4, but for $\varphi_1=30^\circ$.

6 and 7 correspond to a given pair of energies of the two electrons, the left column specifying detection of the first electron with the smallest energy. Moreover, Figs. 6 and 7 display in their right columns an interesting quantity, which we label as “energy-exchange dichroism” ($EE\Delta$), as explained below.

In Fig. 4, when the fixed electron is ejected perpendicularly to the polarization axis, convergence is reached promptly. The final shape of the TDCSs, consisting of two peaks symmetric with respect to back-to-back emission, is obtained already at $R_0=10$ a.u. Only the absolute values show moderate sensitivities to the increase of R_0 , which remain less than 25%.

The TDCSs displayed in Fig. 5, when the fixed electron is ejected at 30° from the electric field, show a slower convergence with R_0 . The shapes obtained at 10 a.u., although not markedly different from the final ones, differ in the details. The peak structure is visible already at $R_0=10$ a.u., yet the

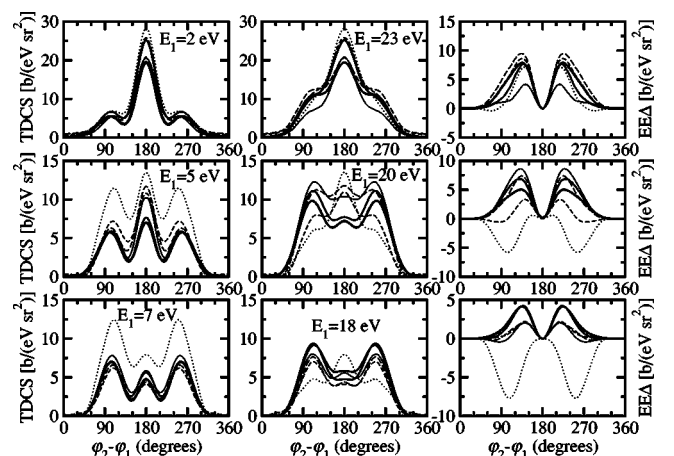


FIG. 6. Left and middle columns: same as Fig. 4, but for $\varphi_1=0^\circ$. Right column: energy-exchange dichroism obtained by subtracting the TDCS plotted in the left column from that plotted in the right one.

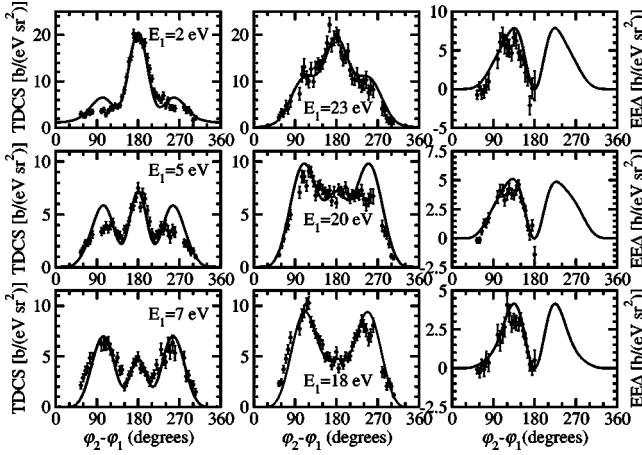


FIG. 7. Same as Fig. 6 but keeping only the $R_0=60$ a.u. HRM-SOW calculations and adding the corresponding present (middle and right columns) and previous [6] (left column) measurements, given by dots with error bars.

ratio of the peaks varies slightly with R_0 , leading to the final structures obtained at $R_0=60$ a.u.: namely, a dominant two-peak structure with a remnant shoulder in the left column, and a dominant one peak structure with two shoulders in the right column. As for the absolute values of the principal peak, their variation with R_0 culminates now at about 40%.

Figure 6 deals with the case when the fixed electron is ejected along the electric-field direction. It exhibits some remarkable cases where the TDCS obtained at $R_0=10$ a.u. are completely at odds with the converged results. At $E_1=18$ and 20 eV, for instance, the shape of the TDCS is dramatically altered when passing from $R_0=10$ to 60 a.u. The ratio of the main peak to the secondary ones is reversed. As a result, the corresponding variation in the peak heights of the TDCSs reaches 100%. In the complementary cases at $E_1=7$ and 5 eV, the TDCSs' shape at $R_0=10$ a.u. is similar to that at $R_0=60$ a.u., yet the absolute values are in error by as much as 75%. Moreover, at $E_1=2, 5, 20,$ and 23 eV, there is still a significant evolution both in the shape and in the magnitude of the TDCSs when going from $R_0=40$ to 50 a.u. This evolution even continues for the most asymmetric energy sharing cases, $E_1=2$ and 23 eV, when going from $R_0=50$ to 60 a.u.; the magnitude of the HRM-SOW TDCSs still varies by about 30%. Comparing Figs. 4–6 provides evidence that the convergence rate of the method slows down when the fixed electron is ejected closer and closer to the electric field. This situation is exacerbated at very asymmetric energy sharing conditions.

The emergence of difficulties when one electron is emitted along the direction of the polarization axis can be understood from the expression of the TDCS in terms of kinematic and dynamic factors. In the experimental conditions of Fig. 7, the latter is given by

$$\sigma^{(3)}(E_1, E_2, \varphi_1, \varphi_2) = |a_g(E_1, E_2, \theta_{12})|(\cos \varphi_1 + \cos \varphi_2) + a_u(E_1, E_2, \theta_{12})|\cos \varphi_1 - \cos \varphi_2|^2, \quad (5)$$

where a_g and a_u are the gerade and ungerade complex dy-

namic amplitudes, symmetric and antisymmetric to the exchange of the two electrons, respectively, and $\theta_{12}=\varphi_2-\varphi_1$. The gerade and ungerade amplitudes both have maximum moduli for back-to-back emission. However, the associated gerade and ungerade kinematic factors have opposite behaviors in this particular geometry: the gerade one is identically zero while the ungerade one reduces to $2 \cos \varphi_1$ and accordingly varies from 0 for $\varphi_1=90^\circ$ or 270° , to ± 2 for $\varphi_1=0$ or 180° . Back-to-back emission, which arises only from the ungerade amplitude, is then magnified when one electron is ejected in the direction of the electric field. Moreover, in these conditions ($\varphi_1=0^\circ$, $\varphi_2=180^\circ$), not only the gerade kinematic factor is zero, but also its first derivative with respect to φ_2 . This defines a φ_2 window where the first term in Eq. (5) almost cancels to zero, allowing one to isolate the second term. The slow convergence of the TDCSs observed at $\varphi_1=0^\circ$ therefore results from a slow convergence of a_u , at least around its maximum corresponding to back-to-back emission.

In addition to the former figures, Fig. 6 exhibits in its right column the $EE\Delta$, defined as

$$EE\Delta(E_1, E_2, \varphi_1, \varphi_2) = \sigma^{(3)}(E_1, E_2, \varphi_1, \varphi_2) - \sigma^{(3)}(E_2, E_1, \varphi_1, \varphi_2). \quad (6)$$

This quantity is not in the strict sense “dichroism,” because it does not appear under any transformation of the incident light, but results from a modification of the dynamics of the two electrons: their energies are exchanged while their directions of emission are kept fixed. It can be observed for any polarization state of the light. This dichroism has already been highlighted by Bolognesi *et al.* at an excess energy of 40 eV [7], in experimental conditions comparable to those of Fig. 7, namely for pure linearly polarized light, a ratio between the individual electronic energies $E_1/E_2=7$ and with one electron detected along the polarization axis.

For the energy pairs (20,5) and (18,7)eV, the $EE\Delta$ is dramatically altered when passing from $R_0=10$ to 60 a.u.: its sign changes throughout the angular range considered. But in all cases, its shape is stabilized by $R_0=20$ a.u., giving rise to two symmetric maxima, the position of which remains almost fixed as R_0 is increased further. By contrast, their magnitude shows important variations, of up to 100% between $R_0=20$ and 60 a.u.

In the experimental conditions of Figs. 6 and 7, the $EE\Delta$ is given by

$$EE\Delta(E_1, E_2, \varphi_1, \varphi_2) = 2|a_g||a_u|\cos(\phi_u - \phi_g) \times (\cos^2 \varphi_1 - \cos^2 \varphi_2), \quad (7)$$

where $|a_g|$, ϕ_g and $|a_u|$, ϕ_u are the moduli and the phases of the gerade and ungerade complex dynamic amplitudes, respectively. The $EE\Delta$ gives information on the relative phase of these two amplitudes. First of all, it does not exhibit, at least in its converged shape, any “dynamic nodes” (i.e., extra zeros, located at angles different from $\theta_{12}=0, 180^\circ$). Second, its simple shape results directly from the competition between the kinematic factor and the product of the two dynamic moduli, so that it implies a monotonic depen-

dence of the relative phase to the mutual angle. Such a property has already been emphasized at an excess energy of 40 eV by Bolognesi *et al.* [29]. The relative phase is even quasiconstant in a large interval of 90° around $\theta_{12}=180^\circ$. The kinematic factor in the energy-exchange dichroism now magnifies an orthogonal emission of the two electrons, allowing one to investigate complementary dynamics to those enlightened by the corresponding TDCSs. The $EE\Delta$ exhibits, for the most asymmetric energy sharing case, significant effects in the vicinity of $\theta_{12}=90^\circ$, indicating that the convergence is particularly slow in the wings of the a_u amplitude. (A forthcoming paper will be devoted to a study of the gerade and ungerade amplitudes.)

Figure 7 compares the converged TDCSs and $EE\Delta$ obtained for $R_0=60$ a.u. with our experimental results. The latter being relative, they have been normalized to the theoretical TDCSs in the nearby vicinity of $\theta_{12}=180^\circ$ for each energy sharing, taking into account the identity of the TDCSs associated with complementary energy patterns for back-to-back emission. Taking advantage of the theoretical symmetry of the energy-exchange dichroism with respect to $\theta_{12}=180^\circ$, the experimental $[0^\circ, 180^\circ]$ and $[180^\circ, 360^\circ]$ $EE\Delta$ have been averaged, so that the corresponding data are only plotted on the $[0^\circ, 180^\circ]$ range.

Special attention should be paid to the measurements presented here at $E_1=20$ eV and 18 eV (middle column of Fig. 7), where the shape of the TDCSs exhibits two peaks linked by a shallow minimum. The HRM-SOW TDCSs calculated at $R_0=60$ a.u. are fully consistent with these data, whereas markedly different shapes were obtained for lower values of R_0 , as already discussed. As a general rule, the overall agreement between theory and experiment is excellent, the exception being the TDCS for $E_1=5$ eV, where the converged theoretical TDCS definitively shows three peaks of comparable magnitude while experiment exhibits a main central peak flanked by two secondary peaks. Assuming that such a disagreement arises from the experiment, we discuss possible sources of systematic errors in the data.

Although the 5 eV distribution is symmetric about $\theta_{12}=180^\circ$, this does not necessarily ensure its reliability, as discussed by Secombe *et al.* [6].² One possibility for the apparent discrepancy is that the “coincidence overlap volume,” as a function of θ_{12} , is not constant in this particular case giving rise to systematic errors in the detection efficiency. This is always a concern of this type of measurement and it is possible that this potential source of error is not completely removed by the normalization procedure (see Secombe *et al.* [6]).

Another factor is the transit of the photon beam through the toroidal analyzer (and entrance lens), which accounts for the absence of data in the angular regions near 90° and 270° . The photon beam is contained within tubes in each of these two regions, to eliminate noise from metal scattered photoelectrons. The presence of these tubes could locally perturb the electric fields within the analyzer. The degree of pertur-

bation is dependent on the tuning of the electron optics, which is different for each electron energy, and could account for the discrepancy between theory and experiment for $E_1=5$ eV, and, to a lesser extent, 2 eV. In principle, the presence of the photon tubes will also perturb the single ionization angular distributions, and therefore, this effect should be removed by the normalization procedure. Nevertheless, it is not impossible that this physical (geometric) difference in the electron optics in the vicinity of 90° and 270° could contribute to the apparent discrepancy.

Such effects (either nonuniformity in the coincidence overlap or photon tube perturbations, or both) are apparent in the TDCSs for $E_1=23, 20,$ and 18 eV, which all have less yield at $\theta_2\sim 240^\circ-270^\circ$ compared to that at $\sim 90^\circ-120^\circ$, the equivalent angular region. Before proceeding we should note that these observations, made in the coplanar geometry, could be due, in part, to nondipole effects. It should also be noted that in cases where the TDCSs’ shape and magnitude are evolving rapidly with E_1/E_2 , as in the $E_1=5$ eV case, it is important to take into account the experimental resolution when comparing theory to experiment. This has been undertaken in this work and the trend is to suppress the yield of the two “side” lobes with respect to the central “peak.” However, this effect changes the TDCS shape by an amount corresponding to the extreme range of the error bars on the data points and consequently does not fully resolve the discrepancy. Nevertheless, these minor differences should not detract from the general consistency between theory and experiment over a wide range of kinematic conditions and where the TDCS shape is markedly changing.

The comparison of the present theoretical TDCSs with the ones published previously (Fig. 3 of Ref. [6]) shows good agreement for the situations $E_1=2$ and 7 eV: namely, the shapes are the same, while the absolute scale varies by less than 25%. However, strong differences both in magnitude and in shape are observed for $E_1=5$ eV, since the magnitude of the main peak varies by as much as 60%, and the ratio of the main peak to the secondary peak alters significantly. In fact, the TDCSs reported in Ref. [6] were obtained with the first version of our method, involving an underlying constant step size α grid in the inner region, and for numerical conditions close to those reported in Fig. 6 for $R_0=30$ a.u.: the present work proves that these data suffered from a lack of convergence with regard to R_0 .

VI. CONCLUSIONS

Reported here is a detailed convergence study of the HRM-SOW method with respect to the critical parameter R_0 that measures the size of the inner region. This study concerns the TDCSs which carry the largest amount of information and which are, accordingly, the most difficult to converge. As a result, the accuracy of HRM-SOW TDCSs has been estimated, for various sizes of the inner region, by the relative deviation of their magnitudes with respect to those calculated at $R_0=60$ a.u. These latter, corresponding to the largest inner region accessible to the present treatment, are taken as a reference because they are in very good agreement with experimental data. At 20 eV, for instance, the accuracy

²Note that for data presented in this work and that of Secombe *et al.* [6] the distance between the hypodermic needle and the detection plane is actually less than 1 mm.

increases from about 25% at $R_0=10$ a.u., to 10% at 40 a.u. and to better than 5% at 50 a.u.

This convergence study has also identified specific situations where the convergence rate becomes particularly slow. They can be distributed in two classes: either very asymmetric energy sharings or emission of one electron close to the electric field in the case of linearly polarized light. In the most asymmetric energy sharing case studied, that is to say $E_1=19.5$ and $E_2=0.5$, so that $E_1/E_2=39$, the accuracy reached at $R_0=50$ a.u. is about 15%. The situation worsens when very asymmetric energy sharing is combined with emission of one electron along the electric field. For $\theta_1=0^\circ$ and $E_1=23$ eV, $E_2=2$ eV, so that $E_1/E_2=11.5$, for instance, the accuracy obtained at $R_0=50$ a.u. cannot be estimated to better than 30%.

Improving the situation requires one either to become able to deal with still larger inner regions or to improve the outer region treatment. In the first case, the obstacle lies in the storage and run-time requirements associated with the diagonalization of a large matrix. To circumvent it, we may consider replacing the general LAPACK diagonalization routine used so far by another one, which would take advantage of the relative sparsity of the relevant matrix. Alternatively, we can explore the capability of the recently developed HTD-SOW method [25], where the stationary inhomogeneous equation (1) is solved over the finite inner region using completely different, namely time-dependent, techniques.

The second option, namely, improving the outer region treatment, is also very promising. The most severe approxi-

mation, in the present implementation, is the description of the main features of the R motion in this region as a single semiclassical outgoing wave. This does not take account of the fact that the R motion might be substantially different in the bulk of the α range $[0, \pi/2]$ interval than in the vicinity of its bounds. Allowing for distinct hyperradial dynamics in the single- and double-ionization channels would probably accelerate the convergence of the HRM-SOW method with respect to R_0 significantly.

The present situation makes additional TDCS measurements very desirable. Accurate absolute TDCSs corresponding to the dynamic situations identified in this paper, i.e., asymmetric energy sharing and/or emission of one electron along the electric field direction for linearly polarized photons, would provide very sensitive tests of the various theories. In addition, PDI of excited 3S helium would help revealing properties of the a_g and a_u dynamic amplitudes, which are hidden when PDI of helium ground state is considered. To conclude, we anticipate that this work will stimulate further experimental and theoretical work in the field.

ACKNOWLEDGMENTS

P.S. and L.M. acknowledge the support of the CNRS computer center IDRIS (Orsay, France) through Project No. 031485. S.A.C., D.P.S., and T.J.R. also acknowledge support from the U.K.'s EPSRC, the European Large Scale Facility Scheme, and LURE.

-
- [1] K. Soejima, A. Danjo, K. Okuno, and A. Yagishita, *Phys. Rev. Lett.* **83**, 1546 (1999).
 - [2] S. Cvejanović, J. P. Wightman, T. J. Reddish, F. Maulbetsch, M. A. MacDonad, A. S. Kheifets, and I. Bray, *J. Phys. B* **33**, 265 (2000).
 - [3] C. Dawson, S. Cvejanović, D. P. Seccombe, T. J. Reddish, F. Maulbetsch, A. Huetz, J. Mazeau, and A. S. Kheifets, *J. Phys. B* **34**, L525 (2001).
 - [4] S. A. Collins, A. Huetz, T. J. Reddish, D. P. Seccombe, and K. Soejima, *Phys. Rev. A* **64**, 062706 (2001).
 - [5] S. A. Collins, S. Cvejanović, C. Dawson, T. J. Reddish, D. P. Seccombe, A. Huetz, L. Malegat, P. Selles, A. K. Kazansky, A. Danjo, K. Soejima, K. Okuno, and A. Yagishita, *Phys. Rev. A* **65**, 052717 (2002).
 - [6] D. P. Seccombe, S. A. Collins, T. J. Reddish, P. Selles, L. Malegat, A. K. Kazansky, and A. Huetz, *J. Phys. B* **35**, 3767 (2002).
 - [7] P. Bolognesi, R. Camilloni, M. Coreno, G. Turri, J. Berakdar, A. S. Kheifets, and L. Avaldi, *J. Phys. B* **34**, 3193 (2001).
 - [8] O. Schwarzkopf and V. Schmidt, *J. Phys. B* **28**, 2847 (1995).
 - [9] H. Bräuning, R. Dörner, C. L. Cocke, M. Prior, B. Krässig, A. S. Kheifets, I. Bray, A. Bräuning-Demian, K. Carnes, S. Dreuil, V. Mergel, P. Richard, J. Ullrich, and H. Schmidt-Böcking, *J. Phys. B* **31**, 5149 (1998).
 - [10] A. Huetz and J. Mazeau, *Phys. Rev. Lett.* **85**, 530 (2000).
 - [11] M. Achler, V. Mergel, L. Spielberger, R. Dörner, Y. Azuma, and H. Schmidt-Böcking, *J. Phys. B* **34**, 965 (2001).
 - [12] L. Malegat, *Phys. Scr., T* **T68**, C113 (2003).
 - [13] T. N. Rescigno, M. Baertschy, W. A. Isaacs, and C. W. McCurdy, *Science* **286**, 2474 (1999).
 - [14] M. Baertschy, T. N. Rescigno, W. A. Isaacs, X. Li, and C. W. McCurdy, *Phys. Rev. A* **63**, 022712 (2001).
 - [15] M. Baertschy, T. N. Rescigno, and C. W. McCurdy, *Phys. Rev. A* **64**, 022709 (2001).
 - [16] J. Colgan, M. S. Pindzola, F. J. Robiccheaux, D. C Griffin, and M. Baertschy, *Phys. Rev. A* **65**, 042721 (2002).
 - [17] J. Röder, M. Baertschy, and I. Bray, *Phys. Rev. A* **67**, 010702(R) (2003).
 - [18] L. Malegat, in *Proceedings of the 23rd International Conference on Photonic, Electronic and Atomic Collisions*, edited by M. Larson *et al.* [Phys. Scr. (to be published)].
 - [19] J. Colgan, M. S. Pindzola, and F. Robiccheaux, *J. Phys. B* **34**, L457 (2001).
 - [20] J. Colgan and M. S. Pindzola, *Phys. Rev. A* **65**, 032729 (2002).
 - [21] L. Malegat, P. Selles, and A. K. Kazansky, *Phys. Rev. Lett.* **85**, 4450 (2000).
 - [22] P. Selles, L. Malegat, and A. K. Kazansky, *Phys. Rev. A* **65**, 032711 (2002).
 - [23] L. Malegat, P. Selles, and A. Kazansky, in *Many-particle Quantum Dynamics in Atomic and Molecular Fragmentation*, edited by J. Ullrich and V. P. Shevelko (Springer, Heidelberg,

- 2003).
- [24] L. Avaldi, *Journal of Radiation Physics and Chemistry* (to be published).
- [25] A. K. Kazansky, P. Selles, and L. Malegat, *Phys. Rev. A* **68**, 052701 (2003).
- [26] J. M. Bizau and F. J. Wuilleumier, *J. Electron Spectrosc. Relat. Phenom.* **71**, 205 (1995).
- [27] F. Citrini, L. Malegat, P. Selles, and A. K. Kazansky, *Phys. Rev. A* **67**, 042709 (2003).
- [28] L. Landau and E. Lifchitz, *Mécanique Quantique* (Mir, Moscow, 1966).
- [29] P. Bolognesi, A. S. Kheifets, I. Bray, L. Malegat, P. Selles, A. K. Kazansky, and L. Avaldi, *J. Phys. B* **36**, L1 (2003).